Lesion Segmentation in Breast Ultrasound Images using Optimized Marked Watershed Method

Xiaoyan Shen
Northeastern University https://orcid.org/0000-0003-4008-7991
He Ma (mahe@bmie.neu.edu.cn)
https://orcid.org/0000-0002-5054-3586
Ruibo Liu
Northeastern University
Hong Li
Northeastern University
Jiachuan He
The First Hospital of China Medical University: The First Affiliated Hospital of China Medical University
Xinran Wu
Northeastern University

Research

Keywords: Breast cancer, Morphology snake, Side window, Ultrasound, Watershed

Posted Date: February 12th, 2021

DOI: https://doi.org/10.21203/rs.3.rs-137797/v2

RESEARCH

Lesion Segmentation in Breast Ultrasound Images using Optimized Marked Watershed Method

Xiaoyan Shen[1], He Ma[1,2*], Ruibo Liu[1], Hong Li[1]
, Jiachuan He[3] and Xinran Wu[1]

*Correspondence:
mahe@bmie.neu.edu.cn
[1]College of Medicine and Biological Information Engineering, Northeastern University, Shenyang, China
Full list of author information is available at the end of the article

Abstract

Background: Breast cancer is one of the most serious diseases threatening women's health. Early screening based on ultrasound can help to detect and treat tumors in early stage. However, due to the lack of radiologists with professional skills, ultrasound based breast cancer screening has not been widely used in rural area. Computer-aided diagnosis (CAD) technology can effectively alleviates this problem. Since Breast Ultrasound (BUS) images have low resolution and speckle noise, lesion segmentation, which is an important step in CAD system, is challenging.

Results: Two datasets were used for evaluation. Dataset A comprises 500 BUS images from local hospitals, while dataset B comprises 205 BUS images from open source. The experimental results show that the proposed method outperformed its related classic segmentation methods and the state-of-the-art deep learning model, RDAU–NET. And its' Accuracy(Acc), Dice efficient(DSC) and Jaccard Index(JI) reached 96.25%, 78.4% and 65.34% on dataset A, and ACC, DC and Sen reached 97.96%, 86.25% and 88.79% on dataset B.

Conclusions: We proposed an adaptive morphology snake based on marked watershed(AMSMW) algorithm for BUS images segmentation. It was proven to be robust, efficient and effective. In addition, it was found to be more sensitive to malignant lesions than benign lesions. What's more, since the Rectangular Region of Interest(RROI) in the proposed method is drawn manually, we will consider adding deep learning network to automatically identify RROI, and completely liberate the hands of radiologists.

Methods: The proposed method consists of two main steps. In the first step, we used Contrast Limited Adaptive Histogram Equalization(CLAHE) and Side Window Filter(SWF) to preprocess BUS images. Therefore, lesion contours can be effectively highlighted and the influence of noise can be eliminated to a great extent. In the second step, we proposed adaptative morphology snake(AMS) as an embedded segmentation function of AMSMW. It can adjust working parameters adaptively, according to different lesions' size. By combining segmentation results of AMS with marker region obtained by morphological method, we got the marker region of marked watershed (MW). Finally, we obtained candidate contours by MW. And the best lesion contour was chosen by maximum Average Radial Derivative(ARD).

Keywords: Breast cancer; Morphology snake; Side window; Ultrasound; Watershed

Background

According to the 2020 global cancer data report, breast cancer has ranked first among the three most common cancers in women, indicating that it has become a serious threat to the health of women worldwide[1]. Studies showed that early detection and diagnosis of breast cancer could effectively increase the cure rate [2]. At present, digital mammography (DM) and breast ultrasound are two main tools used in breast screening in China. However, ultrasound has no ionizing radiation and can show the anatomy and pathology of breast dense tissue, which DM cannot achieve. Therefore, ultrasound is more suitable for detecting breast lesions in Asian women with high density than DM and is becoming a popular screening tool for breast cancer[3]. Geisel *et al.* also demonstrated the effectiveness, practicability and feasibility of breast ultrasound as the screening tool for early detection of occult breast cancer [4]. However, in the process of breast ultrasound imaging, speckle noise generated by coherent waves greatly reduces image quality, which requires a high degree of professionalism for radiologists. Due to the lack of radiologists in remote areas, ultrasound based breast cancer screening can not really be popularized.

With the development of artificial intelligence technology, computer aided diagnosis (CAD) systems based on medical images have made great achievements in cancer detection. Especially, the development of breast cancer CAD system based on Ultrasound is impressive. This will largely alleviate the problem of lack of radiologists. However, due to the inherent characteristics of Breast Ultrasound (BUS) images, as the key step of CAD system, lesion segmentation is challenging. Therefore, to find a stable and effective BUS images segmentation method is of great significance to promote the further development of breast cancer CAD detection system based on breast ultrasound.

In recent years, many excellent image segmentation algorithms have emerged. Level set (LST), first introduced in 1994 [5] and improved in the year of 1995 [6], 2005 [7], 2012 [8] and so on, has been proven to be very effective in image segmentation. However, it needs plenty of time to solve partial deferential equations (PDEs), which is not very practical. In order to solve this problem, morpholical snake (MS) was proposed. It uses morphological operations on a binary level set to approach the differential operators of standard PDE [9]. It only needs numerical calculations. So that MS is simple and fast. In terms of the field of BUS images segmentation, Many scholars [10], [11], [8] used parameter deformable model and geometric deformable model technology. However, for them, in order to achieve ideal segmentation results, an appropriate initial tumor boundary or a precise edge based stop function should be set in advance. Some other researchers have used and improved the graph based segmentation methods [12]and [13]. Boukerroui attempted to overcome the biggest drawbacks of MRF model, i.e., lower optimization speed and local optimization [14]. In 2013, Zhao proposed generalized fuzzy cluster method (FCM) with spatial information, which performs well in segmentation and have a rapid converge speed [15]. FCM and improved FCM algorithm were applied on lesion detection in BUS images [16], [17]. Since 2013, there have been more and more segmentation methods with supervised and semi supervised learning, especially the popularity of deep learning, which has made great progress in solving the problem of BUS images segmentation. The supervised learning includes support vector machine (SVM), artificial neural

network (ANN), Convolutional neural network (CNN), etc., which were applied to BUS images segmentation and made great progress ([18], [19], [20], [21]. Zhuang proposed RDAU-NET model [22], which performs best on BUS images segmentation when compared to other modes. So far, deep learning models have been proven to be the best way to perform image segmentation. However, it faces some major problems, which are also the main bottleneck for the further development. For example, the prediction result is not robust enough, model can't be explainable and training data is not sufficient. In order to solve these problems, a new approach integrated visual saliency into a deep learning model for BUS images segmentation [23]. They introduced attention blocks into a U-Net architecture and learns feature representations that prioritize spatial regions with high saliency levels, and achieved a Dice similarity coefficient (DSC) of 90.5% on a data set of 510 images. However, this method relies much on the quality of saliency maps, which is also not robust enough.

Therefore, how can we have an efficient and robust BUS images segmentation method? We turned to some excellent classic segmentation method again. It is reported that tomography watershed (WS) has a certain effect on solving complex segmentation problems and is more stable compared to other existing methods, but it is sensitive to noise and might cause over-segmentation. In view of this, many scholars have improved WS. Huang and Chen [10] combined WS with the active contour model to obtain a relatively accurate tumor boundary. In 2009, Gomez used marked watershed (MW) algorithm incorporating morphological techniques and average radial derivative (ARD) function [24]. They improved the method by using anistropic diffusion filter (ADF) guided by texture descriptors derived from a set of Gabor filter and creating segmenting function generated by Newton filters to facilitate more precise segmentation [25]. However, ADF needs many iterations to get a good preprocessing result, which takes a long time. In addition, the acquisition of marker function is a little complex, which will reduce the efficiency of the algorithm. In view of these two problems, we have made improvements in previous study [26]. We combined contrast limited adaptive histogram equalization (CLAHE) and curvature filtering (CF) to preprocess images, and used morphological method to obtain the marker function, which is simple and efficient. However, this method not only improves the segmentation accuracy and Dice coefficient, but also brings higher FPR value, which means that many false positive tissues are also segmented. Therefore, to further improve the performance, this paper makes technical contributions, which are concluded into the following three tips.

1. In the image preprocessing part, we use CLAHE and side window filter (SWF) to enhance lesion contour and eliminate the infulence of noise. Compared with some other preprocessing methods, it is the most beneficial to BUS images segmentation.

2. We proposed an embedded segmentation method, adaptive morphological snake (AMS). It is robust and stable when processing complex dataset with different sizes of lesions collected from different types of ultrasound equipment, compared with morphology snake (MS).

3. We proposed an optimized marked watershed segmentation method, adaptive morphology snake based on marked watershed(AMSMW). Its' marker region is corrected by AMS. Taking full consideration of the advantages of classical segmentation algorithm, such as level set (LST) method [5], morphological snake(MS)

[9] and MW [27], we found that AMSMW has higher segmentation precision and also 3-4 times faster than other existing methods.

Results

Evaluation Metrics

We used both area and contour error metrics, which include Accuracy (Acc), true positive ratio (TPR), false positive ratio (FPR), Jaccard index (JI), Dice's coefficient (DSC), area error ratio (AER), Hausdorff error(HE), and mean absolute error (MAE) to do the evaluation on dataset A. The calculation formulas of these indicators are listed as below. In addition, we used Dice coefficient(DC), Area-Under-Curve(AUC), Precision(PC), Sensitivity(Sen), Specificity(Sp), F1score(F1) and Mean-Intersection-Over-Union(M-IOU) to evaluated the proposed method on dataset B. The calculation formulas of these indicators can be referred from Zhuang's paper [22].

$$\mathrm{Acc} = \frac{(A_G \cap A_S) \cup (\mathrm{A} - \mathrm{A_G} \cup \mathrm{A_S})}{\mathrm{A}} \tag{1}$$

$$\mathrm{TPR} = \frac{|A_G \cap A_S|}{|A_G|} \tag{2}$$

$$\mathrm{FPR} = \frac{|A_G \cup A_S - A_G|}{|A_G|} \tag{3}$$

$$\mathrm{JI} = \frac{|A_G \cap A_S|}{|A_G \cup A_S|} \tag{4}$$

$$\mathrm{DSC} = \frac{2\,|A_G \cap A_S|}{|A_G| + |A_S|} \tag{5}$$

$$\mathrm{AER} = \frac{|A_G \cup A_S| - |A_G \cap A_S|}{|A_G|} \tag{6}$$

$$\begin{aligned} &\mathrm{HE}\,(C_G, C_S) = \max\left\{\max_{x \in C_G}\left\{d\,(x, C_S)\right\}\right\}, \max_{x \in C_S}\left\{d\,(y, C_G)\right\} \\ &\text{where, } (z, C) = \min_{k \in C}\{\|z - k\|\} \end{aligned} \tag{7}$$

$$\mathrm{MAE}\,(\mathrm{C_S}, \mathrm{C_G}) = 1/2\left(\sum_{x \in C_S} \frac{d\,(x, C_G)}{n_G} + \sum_{\mathrm{y} \in C_G} \frac{d\,(y, C_S)}{n_S}\right) \tag{8}$$

where A_* is the number of pixels exist inside *, A is the number of all pixels contained in the image, the subscript G and S represent the ground truth and segmentation result, respectively. C represents the contour of ROI. z and k mean the point in the contour.

Xian has mentioned how import these metrics are [12]. JI value is large, and AER, HE and MAE value are small, indicating that the performance is quite good. Suppose that JI is small, when AER, HE, and MAE are large, if TPR and FPR are both large, the lesion was overestimated. And if TPR and FPR are both small, the lesion was underestimated.

Experiment details

In this part, we use Python to implement the algorithm and calculate evaluation metrics. The best parameter setting of AMSMW method is shown in Table 1. Next, we will introduce the process of the three experiments in detail.

finding the most suitable BUS images preprocessing method

We explored the effect of preprocessing methods on segmentation results by using four preprocesing schemes, which include SWF, CLAHE&SWF, CLAHE&CF&SWF, and CLAHE&CF. In addition, we set up a control group without preprocessing operations, in order to prove whether the preprocessing method has influence on the segmentation result.

Comparing AMSMW with other classical image segmentation methods and deep learning methods

Firstly, we used the best preprocessing method obtained by the last step to preprocess 500 BUS images from dataset A. Secondly, we compared the proposed method with some related segmentation methods and RDAU-NET on dataset A. Thirdly, we compared the proposed method with typical deep learning method on dataset B. In terms of traditional segmentation methods, we implemented some related and classical methods, which include LST [5], MS [9], MW [27], FSMW [26], and so on. As for the MS method, we set its initialization position and radius to be the center of the RROI and 70% of the smallest of the length and width of the RROI. Moreover, it is necessary to note that we use the same preprocessing method when doing the comparison experiments expect for FSMW. In terms of deep learning methods, many excellent image segmentation models have been gradually borrowed, improved and used. In the paper [22], several typical deep learning segmentation models are compared on dataset B. The results show that the RADU-NET model performs best. In order to make an objective comparison between AMSMW and RADU-NET, we did the following two experiments. On one hand, we implemented and trained RADU-NET model, using our dataset, which include 1000 BUS images, and performed a quantitative segmentation experiment on dataset A. On the other hand, we performed segmentation experiments on dataset B, using AMSMW.

Studying the sensitivity of AMSMW to benign and malignant lesions

It is considered that benign and malignant tumors are very different in size, morphology, margins, and internal state, which may greatly affect the algorithm's performance. If the relationship can be found, it will be of great significance to design

a more adaptive BUS images segmentation algorithm. Therefore, we conducted an exploratory experiment on the algorithm's sensitivity in segmenting benign and malignant lesions. The specific operation is to firstly group dataset A into 250 benign and 250 malignant groups. and then perform quantitative segmentation experiment.

Experiment results

Combined with CLAHE, SWF can enhance the edge of lesion and contribute to better BUIS segmentation results.

Quantitative result and some examples of qualitative result are shown in Table2 and Figure 1 separately. Firstly, as shown in Table 2, no metrics in the first column is better, indicating that images preprocessing is vital and has a very important effect on the result of BUS images segmentation. Secondly, although the CLAHE&SWF method is lower than SWF method on TPR value, it performs best on the other metrics. This indicates CLAHE can improve the contrast and SWF can smooth the noise, preserving lesion boundary greatly, which can also be seen intuitively from Figure 1.

AMSMW performs best both on quantitative result and qualitative result.

Firstly, some relevant and excellent traditional segmentation methods were tested on dataset A, and the quantitative and qualitative results were shown later. It can be observed from Table 3 that even without the preprocessing method, MW still performs the best on TPR, indicating that MW can segment the entire lesion area more sensitively and comprehensively, whereas the error rate is also raised to the highest, causing too high FPR. That means a large part that does not belong to the lesion area is also segmented, which can be seen intuitively from the qualitative result in Figure 2. Take the images in the third and fourth column for example, a lot of normal tissue were segmented by MW. Whereas, LST has a lower FPR compared to MW, indicating that it can effectively improve the ability of identifying lesion contours. However, other indicators' values of LST are relatively low, indicating that it cannot completely find entire lesion area. Compared with LST, MS has the biggest advantage that it uses morphological methods to replace the process of solving numerical differential equations, improving the efficiency greatly. Through experimental verification, MS is 3 to 4 times faster than LST. At the same time, it can be inferred from the quantitative results that MS is better than LST in most of metrics, indicating that it can segment tumors more precisely than LST. However, as shown in Figure 2, take the third and the fourth column for example. there are some lesions with many calcification points inside, which cannot be segmented completely by MS method, increasing FPR's value. Compared with MS, although AMS is slightly lower than MS on Acc, FPR, AER, HE and MAE, it has obvious advantages on TPR, DSC and JI, showing that AMS is more stable and can get more complete lesions. This is of great significance for obtaining a better maker of AMSMW later. By comparing MS+MW with AMSMW, we find that AMS has great effect on improving the performance. The LST+MW algorithm is a method in which the LST method was used instead of AMS as the embedded segmentation function of MW. By comparing the quantitative results of LST+MW with other methods, it can be found AMSMW has obvious advantages on other indicators

except TPR. In addition, observed from Figure 2, we find that the qualitative result of AMSMW is much closer to GT. Moreover, AMSMW method runs fastest. From all the above, we conclude that AMSMW has highest efficiency and effectiveness. Secondly, we performed segmentation on dataset B shared in the paper[22] and dataset A, respectively. The quantitative and qualitative results are shown in Table 4, Figure 3. and Table 5, Figure 4 , respectively. Observed from Table 5, AMSMW is slightly lower than RDAU-NET on SP, PC and M-IOU, while obviously higher on the other five metrics. This indicates that AMSMW has good adaptability and can segment lesion area more precise than RDAU-NET, which can also be seen more intuitively from Figure 4. It can be inferred from Figure 4, RDAU-NET can also find lesion area, whereas it segments more normal tissue area, increasing FPR's value. Furthermore, from the results of experiment on dataset A, RDAU-NET does not show strong generalization ability, because it is only better than AMSMW on Sen, and is far worse on the other seven metrics. Overall, it is obvious that if there is no enough training data and excellent hardware resources, even the best deep learning model is not available when it comes to new or more complex data. Therefore, there is still a long way for deep learning to go to improve its performance of generalization. In other words, although traditional algorithms cannot be fully automated, the capability of semi-automated is enough to bear doctors' burden, and excellent traditional segmentation algorithms still have good performance when processing complex data.

AMSMW is more sensitive to malignant tumor than benign tumor

As shown in Table 6, the performance of AMSMW in segmenting benign and malignant tumors is comparable. From the four indicators, TPR, DSC, JI and AER, we can conclude that AMSMW is more sensitive to discriminating malignant tumors. However, due to the strong echo behind lesion and the possible strong inner calcification points, AMSMW has a high FPR when segments malignant lesions, causing that the algorithm performs poorly on the other four indicators. Therefore,AMSMW is more stable when segments benign lesions.

Discussion

By exploring the effect of preprocessing methods on segmentation results, we find that the appropriate preprocessing method is conducive to better image segmentation results. For BUS images segmentation with obvious speckle noise, CLAHE & SWF is a better image processing method. By comparing AMSMW with some classic traditional segmentation methods, we find that AMSMW is the most efficient and effective alogrithm. This is mainly because AMS method can adaptively change the working parameters without tedious calculation of the PED equation as the embbeded segmentation function. By comparing AMSMW with the state-of-the-art deep learning models, RDAU-NET and U-NET and so on, AMSMW still performed well on most of the metrics. It proves that AMSMW has strong robustness as a semi-automatic segmentation algorithm. While RDAU-NET has the ability of automatic segmentation, it has weak generalization ability. When dealing with complex images with more speckle noise, different shapes and sizes of tumor and from different ultrasonic equipment, RDAU-NET is far less powerful than AMSMW.

The main reason is that the labeled training set is limited and the learning ability of the model is limited. However, in present era of deep learning, which has attracted much attention and is widely sought after, most of the deep learning models do not have the ideal generalization ability, which leads to the bottleneck of its continuous development. Wheras, the traditional segmentation method is stable and efficient, which provides a way to solve the bottleneck problem of deep learning to a certain extent. Therefore, in the future work, we should not abandon classical segmentation methods. Probably, it is a great solution to integrate the efficient and stable traditional segmentation method with deep learning model to complete images segmentation work, and the results will certainly be greatly improved. By evaluating the sensitivity of the algorithm in segmenting benign and malignant tumors, we get that AMSMW has high sensitivity for the delineation of malignant tumor boundary, and is relatively stable for benign tumor. Therefore, in the future work, we could take the strong echo and characteristics of malignant tumor into account, and set up an adaptive ideal segmentation method.

Conclusions

In this paper, an efficient semi-automatic BUS images segmentation method was proposed and evaluated quantitatively. It was proven to be the most robust and effective BUS images segmentation method than classic traditional segmentation methods and the-state-of-the-art deep learning model. In addition, by studying the sensitivity of AMSMW in segmenting benign and malignant lesions, we find that it is more sensitive to malignant lesions and more stable to benign lesions, which is of great significance to the algorithm research of precision medicine in the future. What's more, since the RROI in the proposed method is drawn manually, we will consider adding deep learning network to automatically identify RROI, and completely liberate the hands of radiologists.

Methods

The flowchart of the proposed method, AMSMW, is shown in Figure 5. It is mainly consisted with four parts: data acquisition, RROI Acquisition, Image preprocessing, marker acquisition and final contour acquisition. The specific steps of each part are listed in the frame.

Data Acquisition

Dataset A was collected by us. It has 500 BUS images, which include 250 benign solid cysts and 250 malignant solid cysts. They are captured from different devices, such as GE LOGIQ E9 and PHILIPS EPIQ 5, in the local hospital. The patient information on all images were hidden. An experienced radiologist sketched lesion boundary for each image as the ground-truth (GT). Dataset B is shared by the open source of the paper [22].

RROI Acquisition

RROI(rectangular region of interest) is obtained manually by the following step: firstly, selecting a point as a starting point by left-clicking the mouse, holding down the left mouse button to move diagonally until the end position is found. Here,

we define the RROI's four vertices as w_1,w_2, h_1, and h_2, respectively, where w and h represent the point is along the tumor's width and height, respectively, and subindices 1 and 2 represent the lower and upper limits of the tumor's width and height, respectively. The geometric center of the RROI, which will be used later, can be defined as

$$\hat{\mu} = (\mu_w, \mu_k) = \left(w_1 + \frac{w_2 - w_1}{2}, h_1 + \frac{h_2 - h_1}{2} \right) \tag{9}$$

Image Pre-processing

Contrast Enhancement

BUS images are characterized by low-contrast and much noise, which can be improved by applying CLAHE, an optimization method based on adaptive histogram equalization(AHE) by limiting the increase in contrast. It excellently overcomes the problem of over-amplifying noise that AHE algorithm has.

Edge Highlighting

Local windows, whose center of the window aligned with the pixels being processed, usually causes blurred edges. In order to avoid this, [28] proposed SWF, which can significantly preserve edges. Thus, we introduced SWF to highlight lesions'edges in BUS images. We will give a brief introduction on SWF, more can be found in the paper [28].

As shown in Figure 6, eight side windows are only defined in a discrete case, where (x, y) is the coordinates of target pixel i, r and θ are the radius and angle of the window, respectively. $\rho \in \{o,r\}$, $\theta = k \times \pi/2$, $k \in [0,3]$. Thus, we can get four side windows,W_{Di},W_{Ri}, W_{Ui} and W_{Li}, by setting ρ=r , which align i with their sides. While ρ=0, we have W_{SWi},W_{SEi}, W_{NEi} and W_{NWi}, which align i with their corners. For each pixel, the process of filtering can be regarded as the process of finding the I_{am} value, which satisfies:

$$I_{\mathrm{m}} = \arg\min_{n \in S} \|q_i - I_n\|_2^2 \tag{10}$$

where,

$$\begin{aligned} \mathrm{I}_n &= \tfrac{1}{N_n} \textstyle\sum_{j \in w_i^n} w_{ij} q_j \\ \mathrm{N}_n &= \textstyle\sum_{j \in w_i^n} w_{ij}, n \in S \end{aligned} \tag{11}$$

W_{ij} is the weight of pixel j, which is neighbored with pixel i, based on the filtering kernel F, q_j is the intensities of image q at location i, and S=L, R, U, D, NW, NE, SW, SE is the set of side window index. The result of filtering by SWF is defined as:

$$\mathrm{I}'_{\mathrm{SWF}} = \arg \min_{\forall I_i^{\theta,\rho,r}} \left\| q_i - I_i^{\prime\theta,\rho,r} \right\|_2^2 \tag{12}$$

where

$$\mathrm{I}_i^{\prime\theta,\rho,r} = F\left(q_i, \theta, \rho, r\right) \tag{13}$$

$I_i^{'\theta,\rho,\gamma}$ is the result of eight side windows, when $\rho \in \{o,r\}$, $\theta = k \times \pi/2$, $k \in [0,3]$.

Constraint Gaussian kernel set

Similar to the method proposed in the paper [26], We multiply Gaussian functions with the filtered image I_{CF} to obtain the region of interest(ROI). Whereas the difference is we used a union of five constrained Gaussian, which have the same variances, in order to make the lesion area more prominent.

$$\sigma_w = \frac{w_2 - w_1}{2}, \sigma_h = \frac{h_2 - h_1}{2} \tag{14}$$

The only difference between the five constrained Gaussian functions is the center position. One is centered at the geometric center of the RROI, and the other four are translated by half of diagonal lengths to the four diagonal directions of the RROI, respectively. Hence, take the Gaussian function which centered at the geometric center of the RROI as an example, its function could be expressed as

$$G(m,n) = \frac{\exp\left(-\mathbf{1/2}\left(\frac{(\hat{p}-\hat{\mu})^2}{\sigma_w^2} + \frac{(\hat{p}-\hat{\mu})^2}{\sigma_h^2}\right)\right)}{2\pi\sqrt{\det s_\sigma}} \tag{15}$$

where $\hat{p}$(m,n) represents the pixel's location, s_α is the diagonal covariance matrix. It could be expressed as:

$$s_\sigma = \begin{pmatrix} \sigma_w^2 & 0 \\ 0 & \sigma_h^2 \end{pmatrix} \tag{16}$$

Referring to (7), We superimpose these five Gaussian functions to obtain their union G_T, and then multiply it with I_{CF}, which was negative firstly.

$$J(m,n) = G_T(m,n) \bullet \left(\mathbf{1} - \frac{I_{CF}(m,n)}{\max_{\hat{p}}\left(I_{CF}(m,n)\right)}\right) \tag{17}$$

Therefore, a specially highlighted ROI, whose surrounding tissue is greatly darkened, is obtained as shown in Figure 7. Experiments shows that the illuminated ROI obtained by these five Gaussian function sets are more complete than before, which is significant for determining accurate tumor boundaries and performing efficient segmentation.

Opening operation

The input image of marker function, JmnM, and the input image of segmentation function, JmnN are obtained separately by performing opening operation on J using 9 pixels disk and 15 pixels radius disk, respectively.

Marker Acquisition

The marker region of AMSMW is obtain by taking the intersection of mark function and partition function.

Marker function

Similiar to the paper [26], we get the marker function through a series of morphological operations. Firstly, We binarize JmnM with 1-255 as the threshold, respectively. And the 255 binarized images are denoted asf_p^{th}(m,n), (th=1,2,...,255), corresponding to 255 marker functions. Referring to (8), maker function can be obtained by performing morphology operation.

$$\begin{gathered} f_{Mar}^{th}(m,n) = f_{ext}^{th}(m,n) \cup f_{int}^{th}(m,n) \\ \text{where} \quad f_{ext}^{th}(m,n) = \delta_{B_2}\left(\delta_{B_1}\left(f_p^{th}(m,n)\right)\right) - \varepsilon_{B_2}\left(\delta_{B_1}\left(f_p^{th}(m,n)\right)\right) \\ \text{and} \quad f_{int}^{th} = \varepsilon_{B_1}\left(f_p^{th}(m,n)\right) \end{gathered} \tag{18}$$

where f_p^{th} represents the marker function;f_{ex}^{th} and f_{in}^{th} represent the external and internal markers, respectively. and δ and ε are morphological dilation and erosion, respectively; B_1 and B_2 are two structure elements with 15 pixels radius disk and pixel square, respectively.

Segmentation function

In the paper [26], we discussed and proved that the segmentation function plays a great role in whether we can obtain accurate markers, and has a great contribution to obtain good segmentation results. Therefore, to get more precise segmentation result, we evaluate the existing segmentation methods and proposed an optimized method to obtain the segmentation function.

(1)MS: Let u_e: $R^+ \times R^2 \rightarrow$R be an implicit representation of C such that C(t)=(x,y); u(t,(x,y))=0. MS uses a combination of binary morphological operators whose infinitesimal behavior is equivalent to the flow expressed by the active contour PDE(9). Therefore, the curve is given as the zero level set of a binary piecewise constant function u: $R^2 \rightarrow \{0,1\}$. We take u(x)=1 for every point x inside the curve, and u(x)=0 for every point x outside the curve. The morphological operators will act on u and will implicitly evolve the curve.

$$\frac{\partial u}{\partial t} = g(I)|\nabla u|\left(div\left(\frac{\nabla u}{|\nabla u|}\right) + v\right) + \nabla g(I)\nabla u \tag{19}$$

where v$\in$ R is the balloon force parameter and g(I) selects which regions of I attract the curve. In the MS model, we used two common morphological operators, which are erosion and dilation. The dilation of a function is defined as:

$$\left(D_h u\right)(\mathrm{x}) = \sup_{y \in hB} u(\mathrm{x} - \mathrm{y}) \tag{20}$$

The erosion is defined as

$$\left(E_h u\right)(\mathrm{x}) = \inf_{y \in hB} u(\mathrm{x} - \mathrm{y}) \tag{21}$$

The balloon force PDE can be expressed as

$$\frac{\partial u_{ball}}{\partial t} = g(I) \bullet V \bullet |\nabla u_{ball}| \tag{22}$$

Given that the snake evolution at iteration n, u^n: $R^2 \rightarrow \{0,1\}$, it can be solved using the following morphological approach:

$$u^{n+1}(x_i) = \begin{cases} (D_d u^n)(x_i) & \text{if } g(I)(x_i) > \theta \text{ and } v > 0 \\ (E_d u^n)(x_i) & \text{if } g(I)(x_i) > \theta \text{ and } v < 0 \\ u^n(x_i) & \text{otherwise} \end{cases} \tag{23}$$

Where D_d and E_d are the discrete versions of dilation and erosion. Therefore, the morphological implementation of (13) can be expressed as:

$$u^{n+\frac{1}{3}}(x) = \begin{cases} (D_d u^n)(x_i) & \text{if } |v| g(I)(x_i) > \theta \text{ and } v > 0 \\ (E_d u^n)(x_i) & \text{if } |v| g(I)(x_i) > \theta \text{ and } v < 0 \\ u^n(x_i) & \text{otherwise} \end{cases} \tag{24}$$

$$u^{n+\frac{2}{3}}(x_i) = \begin{cases} 1 & \text{if } \nabla u^{n+\frac{1}{3}} \nabla g(I)(x_i) > 0 \\ 0 & \text{if } \nabla u^{n+\frac{1}{3}} \nabla g(I)(x_i) < 0 \\ u^{n+\frac{1}{3}} & \text{if } \nabla u^{n+\frac{1}{3}} \nabla g(I)(x_i) = 0 \end{cases} \tag{25}$$

$$u^{n+1}(x_i) = \begin{cases} SI_d \circ IS_d u^{n+\frac{2}{3}}(x_i) & \text{if } \quad g(I)(x) > 0 \\ u^{n+\frac{2}{3}}(x) & \text{otherwise} \end{cases} \tag{26}$$

where SI_d and IS_d are smoothing operators. In binary images u, SI_d works only on white pixels and IS_d works only on black pixels. Take SI_d for example, for every white pixel x_1 in a binary image, the SI_d operator looks for small (3 pixels long) straight lines of white pixels which contain x_1. This search is done in the four possible orientations corresponding to the four segments in P, where P is a collection of four discretized segments centered at the origin.

$$P = \begin{Bmatrix} \{(0,0), & (1,0), & (-1,0)\}, \\ \{(0,0), & (1,1), & (0,-1)\}, \\ \{(0,0), & (0,1), & (-1,-1)\}, \\ \{(0,0), & (1,-1), & (-1,1)\}, \end{Bmatrix} \tag{27}$$

If no straight line exists, the pixel is made black (see Figure 8). Sharp edges (Figure 8b and Figure 8d) are detected and removed as those pixels which aren't part of a straight line. The white pixels in smooth edges (Figure 8a and Figure 8c) remain unchanged.

If no straight line exists, the pixel is made black (see Figure 8). Sharp edges (Figure 8b and 8d) are detected and removed as those pixels which aren't part of a straight line. The white pixels in smooth edges (Figure 8a and Figure 8c) remain unchanged.

(2)AMS: Considering the different size of tumor in our dataset, MS is not sensitive to especially large or small tumor. Therefore, we propose AMS, which is a optimized model based on MS model, by applying some adjustments on choosing appropriate parameters.

In the AMS model, different shapes and nature of tumors are considered. We use the geometric center of the manually acquired RROI as initial point, and adjust the radius and iterations of the circle level set in real time according to the aspect ratio of the tumor, Whereas in MS model, these parameters are fixed. Table 6 lists the relevant adjustable parameters of MS and AMS.

Finally, we can find the minimum boundary fsmth(m, n), referring to (18). Then, we obtained the maker of MW, , by performing closing operation with 25 pixels radius disk after binarization.

$$f_{sm}^{th}(m,n) = f_{seg}(m,n) \cap f_{mar}^{th}(m,n) \tag{28}$$

Final contour acquisition

Firstly, we get 255 candidate contours by putting f_{label}^{th}(m, n) as the input of MW,referring to (19).

$$f_{\mathrm{MW}}^{th}(m,n) = \mathrm{MW}\left(f_{\mathrm{label}}^{th}(m,n)\right) \tag{29}$$

Secondly, We take the contour corresponding to the largest ARD as the final one. In order to improve the efficiency of the algorithm and ensure that the selected boundary line is close to the ideal boundary line, we directly take the candidate boundary corresponding to threshold 96 as the final contour line, thus avoiding the calculation of ARD for 255 candidate boundaries in an image. (More details, please refer to paper [26]).

Abbreviations

BUS: Breast Ultrasound CLAHE: Contrast Limited Adaptive Histogram Equalization SWF: Side Window Filter RROI: Rectangular Region of Interest AMS: Adaptative Morphology Snake ARD: Average Radial Derivative MW: marked watershed

Declarations

Ethics approval and consent to participate
This study was approved by the Medical Ethics Committee of the First Hospital of China Medical University and was in accordance with the 1964 Helsinki declaration and its later amendments or comparable ethical standards. All subjects gave written informed consent in accordance with the Declaration of Helsinki.

Consent for publication
Not applicable.

Availability of data and materials
The datasets analyzed during the current study are available from the corresponding author on reasonable request.

Competing interests
The authors declare that they have no competing interests.

Funding
This research is supported in part by the National Natural Science Foundation of China under Grant No. 61702087 and in part by the Fundamental Research Funds for the Central Universities under Grant No. N172008008.

Authors' contributions

XS carried out the algorithm design and implementation, and drafted the manuscript. HM participated in the design of the study, coordination and contributed suggestions to complete the manuscript. RL implemented RDAU-NET. HL contributed to discussions. JH participated in collecting data and delineating tumors. XW participated in discussion, organizing data and writing formulas with latex code. All authors read and approved the final manuscript

Acknowledgements

Not applicable

Authors' information

Author details

[1]College of Medicine and Biological Information Engineering, Northeastern University, Shenyang, China. [2]Key Laboratory of Intelligent Computing in Medical Image, Ministry of Education, China. [3]Department of radiology, Liaoning Cancer Hospital, Shenyang, China.

References

1. Siegel, R.L., Miller, K.D., Jemal, A.: Cancer statistics, 2020. CA: A Cancer Journal for Clinicians **70**(1), 7–30 (2020). doi:10.3322/caac.21590
2. Jemal, A., Bray, F., Center, M.M., Ferlay, J., Ward, E., Forman, D.: Global cancer statistics. CA: a cancer journal for clinicians **61**(2), 69–90 (2011)
3. Drukker, K., Giger, M.L., Horsch, K., Kupinski, M.A., Vyborny, C.J., Mendelson, E.B.: Computerized lesion detection on breast ultrasound. Medical Physics **29**(7), 1438–1446 (2002). doi:10.1118/1.1485995
4. Geisel, J., Raghu, M., Hooley, R.: The Role of Ultrasound in Breast Cancer Screening: The Case for and Against Ultrasound. Seminars in ultrasound, CT, and MR **39**(1), 25–34 (2018). doi:10.1053/j.sult.2017.09.006
5. Sussman, M.: A level set approach for computing solutions to incompressible two-phase flow. Journal of Computational Physics **114**(1), 146–159 (1994). doi:10.1006/jcph.1994.1155
6. Adalsteinsson, D., Sethian, J.A.: A fast level set method for propagating interfaces. Journal of computational physics **118**(2), 269–277 (1995)
7. Shi, Y., Karl, W.C.: Real-time tracking using level sets. In: 2005 IEEE Computer Society Conference on Computer Vision and Pattern Recognition (CVPR'05), vol. 2, pp. 34–41 (2005). IEEE
8. Gao, L., Liu, X., Chen, W.: Phase- and GVF-based level set segmentation of ultrasonic breast tumors. Journal of Applied Mathematics **2012** (2012). doi:10.1155/2012/810805
9. Álvarez, L., Baumela, L., Henríquez, P., Márquez-Neila, P.: Morphological snakes. Proceedings of the IEEE Computer Society Conference on Computer Vision and Pattern Recognition, 2197–2202 (2010). doi:10.1109/CVPR.2010.5539900
10. Huang, Y.L., Jiang, Y.R., Chen, D.R., Moon, W.K.: Watershed segmentation for breast tumor in 2-D sonography. International Journal of Computer Assisted Radiology and Surgery **1**(SUPPL. 7), 63–65 (2006). doi:10.1007/s11548-006-0044-6
11. Gómez, W., Infantosi, A.F.C., Leija, L., Pereira, W.C.A.: Active contours without edges applied to breast lesions on ultrasound. IFMBE Proceedings **29**(2), 292–295 (2010). doi:10.1007/978-3-642-13039-7-73
12. Xian, M., Zhang, Y., Cheng, H.D.: Fully automatic segmentation of breast ultrasound images based on breast characteristics in space and frequency domains. Pattern Recognition **48**(2), 485–497 (2015). doi:10.1016/j.patcog.2014.07.026
13. Chiang, H.H., Cheng, J.Z., Hung, P.K., Liu, C.Y., Chung, C.H., Chen, C.M.: Cell-based graph cut for segmentation of 2D/3D sonographic breast images. 2010 7th IEEE International Symposium on Biomedical Imaging: From Nano to Macro, ISBI 2010 - Proceedings, 177–180 (2010). doi:10.1109/ISBI.2010.5490384
14. Boukerroui, D., Basset, O., Guérin, N., Baskurt, A.: Multiresolution texture based adaptive clustering algorithm fo breast lesion segmentation. European Journal of Ultrasound **8**(2), 135–144 (1998). doi:10.1016/S0929-8266(98)00062-7
15. Zhao, F., Jiao, L., Liu, H.: Kernel generalized fuzzy c-means clustering with spatial information for image segmentation. Digital Signal Processing: A Review Journal **23**(1), 184–199 (2013). doi:10.1016/j.dsp.2012.09.016
16. Lo, C., Shen, Y.W., Huang, C.S., Chang, R.F.: Computer-aided multiview tumor detection for automated whole breast ultrasound. Ultrasonic Imaging **36**(1), 3–17 (2014). doi:10.1177/0161734613507240
17. Moon, W.K., Lo, C.M., Chen, R.T., Shen, Y.W., Chang, J.M., Huang, C.S., Chen, J.H., Hsu, W.W., Chang, R.F.: Tumor detection in automated breast ultrasound images using quantitative tissue clustering. Medical Physics **41**(4) (2014). doi:10.1118/1.4869264
18. Liu, B., Cheng, H.D., Huang, J., Tian, J., Tang, X., Liu, J.: Fully automatic and segmentation-robust classification of breast tumors based on local texture analysis of ultrasound images. Pattern Recognition **43**(1), 280–298 (2010). doi:10.1016/j.patcog.2009.06.002
19. Huang, S.F., Chen, Y.C., Woo, K.M.: Neural network analysis applied to tumor segmentation on 3D breast ultrasound images. 2008 5th IEEE International Symposium on Biomedical Imaging: From Nano to Macro, Proceedings, ISBI **i**, 1303–1306 (2008). doi:10.1109/ISBI.2008.4541243
20. Xu, Y., Wang, Y., Yuan, J., Cheng, Q., Wang, X., Carson, P.L.: Medical breast ultrasound image segmentation by machine learning. Ultrasonics **91**(March 2018), 1–9 (2019). doi:10.1016/j.ultras.2018.07.006
21. Ronneberger, O., Fischer, P., Brox, T.: U-net: Convolutional networks for biomedical image segmentation. In: International Conference on Medical Image Computing and Computer-assisted Intervention, pp. 234–241 (2015). Springer
22. Zhuang, Z., Li, N., Joseph Raj, A.N., Mahesh, V.G., Qiu, S.: An rdau-net model for lesion segmentation in breast ultrasound images. PloS one **14**(8), 0221535 (2019)
23. Vakanski, A., Xian, M., Freer, P.E.: Attention-enriched deep learning model for breast tumor segmentation in ultrasound images. Ultrasound in Medicine & Biology **46**(10), 2819–2833 (2020)

24. Gómez, W., Leija, L., Pereira, W.C.A., Infantosi, A.F.C.: Morphological operators on the segmentation of breast ultrasound images. 2009 Pan American Health Care Exchanges - PAHCE 2009, 67–71 (2009). doi:10.1109/PAHCE.2009.5158367
25. Gómez, W., Leija, L., Alvarenga, A.V., Infantosi, A.F.C., Pereira, W.C.A.: Computerized lesion segmentation of breast ultrasound based on marker-controlled watershed transformation. Medical Physics **37**, 82–95 (2010). doi:10.1118/1.3265959
26. Shen, X., Liu, J., Li, H., Sun, H., Ma, H.: A novel lesion segmentation method based on breast ultrasound images. ACM International Conference Proceeding Series, 32–38 (2019). doi:10.1145/3366174.3366176
27. Lewis, S.H., Dong, A.: Detection of breast tumor candidates using marker-controlled watershed segmentation and morphological analysis. In: 2012 IEEE Southwest Symposium on Image Analysis and Interpretation, pp. 1–4 (2012). IEEE
28. Yin, H., Gong, Y., Qiu, G.: Side window filtering. In: Proceedings of the IEEE Conference on Computer Vision and Pattern Recognition, pp. 8758–8766 (2019)

Figures

Figure 1 Some examples of the effect of different preprocess methods. From the first row to the last row are the result of CCS(contrast limited adaptive histogram equalization+curvature filter+side window filter), CC(contrast limited adaptive histogram equalization+curvature filte), CS(contrast limited adaptive histogram equalization+side window filter) and SWF(side window filter) respectively.

Figure 2 From up to down are the qualitative result of MW(markerd watershed), LST(level set), MS(morphological snake), AMS(adaptive morphological snake), MS+MW(morphological snake and marked watershed), AMSMW(Adaptive morphological snake and marked watershed), LST+MW(level set and marked watershed), FSMW and GT(ground truth)

Figure 3 The qualitative segmentation result. The first row is GT and the second row is the qualitative result of AMSMW on the shared database. And from left to the right are image(a), image(b), image(c), image(d), image(e), image(f), image(g), image(h), image(i), image(j), image(k) and image(l). All of them can be found in the figure11,figure12 and figure 13 of Zhuang's paper ([22]) accordingly.

Figure 4 From up to down are the qualitative result of RADU-NET and GT, respectively.

Figure 5 Flowchart of the proposed method

Figure 6 Definition of side window. r is the radius of the window. (a) side window in continuous case. (b) The left (L) and right (R) side window. (c) The up (U) and down (D) side window. (d) The northeast (NE), northwest (NW), southeast (SE) and southwest (SW) side window.

Figure 7 The process of obtaining ROI(region of interest). (a) original image with RROI(rectangle region of interest) draw by hands; (b) a constrained Gaussian function centered at the geometric center of RROI; (c) resultant image after multiplying (b) and (d); (d) negative of I_{CF}; (e) the union of five constrained Gaussian functions; (f)resultant image, which is denoted as J, after multiplying (e) and (d).

Tables

Figure 8 Some example of the effect of the SI_d and Id_S operator. It keeps unchanged where a straight line(marked in red) is found, as shown in (a) and (c). However, when the center point isn't in any straight line, it will be changed as shown in (b) and (d)

Table 1 The optimal parameters value of the AMSMW method.

method	initial point	Radius and iterations
AMSMW	the geometric center of RROI	$\mathrm{R} = \mathrm{w} - 20, \text{iterations} = 250, \text{if} \min(\mathrm{h}, \mathrm{w}) > 20, \text{ and } \mathrm{h} > 1.5\mathrm{w}$; $\mathrm{R} = \mathrm{w} - 20, \text{iterations} = 120, \text{if} \min(\mathrm{h}, \mathrm{w}) > 20, \text{and } \mathrm{w}/1.5 < \mathrm{h} < 1.5\mathrm{w}$; $\mathrm{R} = \mathrm{w} - 10, \text{iterations} = 250, \text{if} \min(\mathrm{h}, \mathrm{w}) < 20, \text{and } \mathrm{h} > 1.5\mathrm{w}$; $\mathrm{R} = \mathrm{w} - 10, \text{iterations} = 120, \text{if} \min(\mathrm{h}, \mathrm{w}) < 20, \text{and } \mathrm{w} < \mathrm{h} < 1.5\mathrm{w}$; $\mathrm{R} = \mathrm{w} - 10, \text{iterations} = 120, \text{if} \min(\mathrm{h}, \mathrm{w}) < 20, \text{and } 0 < \mathrm{h} < \mathrm{w}$

Table 2 the quantitative result of exploring the effect of preprocessing methods on segmentation results. (CC:CLAHE+CF; CCS: CLAHE+CF+SWF; CS: CLAHE+SWF* Values are the average (±standard deviation) for 500 images)

	None	SWF	CC	CCS	CS
Acc(%)	94.48 (±0.04)	95.35 (±0.04)	96.25 (±0.03)	96.19 (±0.03)	**96.59** (±0.03)
TPR(%)	91.323 (±0.12)	**92.57** (±0.08)	0.9004 (±0.09)	89.11 (±0.09)	83.29 (±0.09)
FPR(%)	59.57 (±0.19)	53.14 (±0.17)	41.90 (±0.18)	41.92 (±0.18)	**1.94** (±0.17)
DSC(%)	73.25 (±0.08)	76.23 (±0.08)	78.39 (±0.08)	77.86 (±0.08)	**78.40** (±0.08)
JI(%)	58.36 (±0.09)	62.25 (±0.10)	65.17 (±0.11)	64.48 (±0.11)	**65.34** (±0.11)
AER(%)	68.25 (±0.26)	60.56 (±0.30)	51.86 (±0.30)	52.81 (±0.29)	**46.45** (±0.26)
HE	66.37 (±32.01)	60.90 (±31.27)	54.36 (±28.94)	54.65 (±28.61)	**51.33** (±29.54)
MAE	26.12 (±11.12)	22.36 (±9.20)	18.77 (±7.30)	19.15 (±7.26)	**17.70** (±7.65)

Table 3 the quantitative result of different segmentation methods.

	ACC (%)	TPR (%)	FPR (%)	DSC (%)	JI (%)	AER (%)	HE	MAE
MW	94.37 (±0.03)	**97.64** (±0.02)	79.17 (±0.05)	71.80 (±0.08)	56.68 (±0.10)	81.53 (±0.41)	69.21 (±26.97)	27.88 (±8.81)
LST	94.69 (±0.03)	95.56 (±0.05)	5.24 (±0.03)	69.58 (±0.13)	54.83 (±0.14)	98.11 (±0.78)	72.54 (±26.35)	28.09 (±9.06)
MS	95.76 (±0.04)	63.05 (±0.13)	11.93 (±0.16)	71.57 (±0.10)	56.72 (±0.12)	48.88 (±0.17)	69.91 (±50.21)	22.68 (±13.67)
AMS	94.38 (±0.05)	81.70 (±0.15)	45.32 (±0.28)	72.69 (±0.09)	58.01 (±0.11)	63.62 (±0.32)	72.72 (±44.87)	24.94 (±14.53)
MS+MW	95.92 (±0.03)	67.65 (±0.04)	15.40 (±0.11)	73.57 (±0.12)	59.14 (±0.14)	47.74 (±0.73)	67.00 (±25.24)	21.75 (±7.13)
AMSMW	**96.59** (±0.02)	83.29 (±0.11)	**1.94** (±0.21)	**78.40** (±0.09)	**65.34** (±0.11)	**46.45** (±0.22)	**51.33** (±28.66)	**17.70** (±7.37)
LST+MW	96.25 (±0.03)	91.58 (±0.06)	50.52 (±0.20)	77.47 (±0.09)	64.18 (±0.12)	58.94 (±0.45)	55.85 (±27.01)	19.50 (±7.36)
FSMW	96.19 (±0.03)	92.88 (±0.05)	52.19 (±0.14)	77.53 (±0.09)	64.27 (±0.12)	59.30 (±0.45)	56.08 (±28.61)	19.50 (±7.21)

Table 4 the quantitative result of AMSMW on the database shared by paper [22]

	loss (%)	Acc (%)	DC (%)	Sen (%)	Sp (%)	F1 (%)	Pc (%)	M-IOU (%)
UNet	17.95	97.57	82.04	84.66	98.91	82.11	81.85	79.83
RDAU	15.30	97.91	84.69	83.19	**99.34**	84.78	**88.58**	**80.67**
AMSMW	**13.75**	**97.96**	**86.25**	**88.79**	98.32	**86.25**	86.26	76.73

Table 5 the quantitative result of AMSMW on our database.

	loss (%)	Acc (%)	DC (%)	Sen (%)	Sp (%)	F1 (%)	Pc (%)	M-IOU (%)
RDAU	36.73	92.65	63.27	**92.35**	92.62	63.27	52.43	49.45
AMSMW	**21.60**	**96.59**	**78.40**	83.29	**97.21**	**78.40**	**75.48**	**65.34**

Table 6 the quantitative result of study on algorithm's sensitivity in segmenting benign and malignant tumors. (B: Benign tunor; M: malignant tumor)

	ACC (%)	TPR (%)	FPR (%)	DSC (%)	JI (%)	AER (%)	HE	MAE
B	**97.46**	79.54	**1.94**	76.24	62.63	50.03	**42.15**	**15.71**
M	95.71	**87.03**	3.65	**80.55**	**68.05**	**42.87**	60.51	19.68

Table 7 The adjustable parameters of MS(morphological snake) and AMS(adaptive morphological snake).

method	initial point	Radius	iterations
MS	A fixed point (default to be the center of the image)	A fixed value (default to be 75% of the smallest image dimension)	a fixed value
AMS	the geometric center of RROI	Real-time adjusted value	Real-time adjusted value

Figures

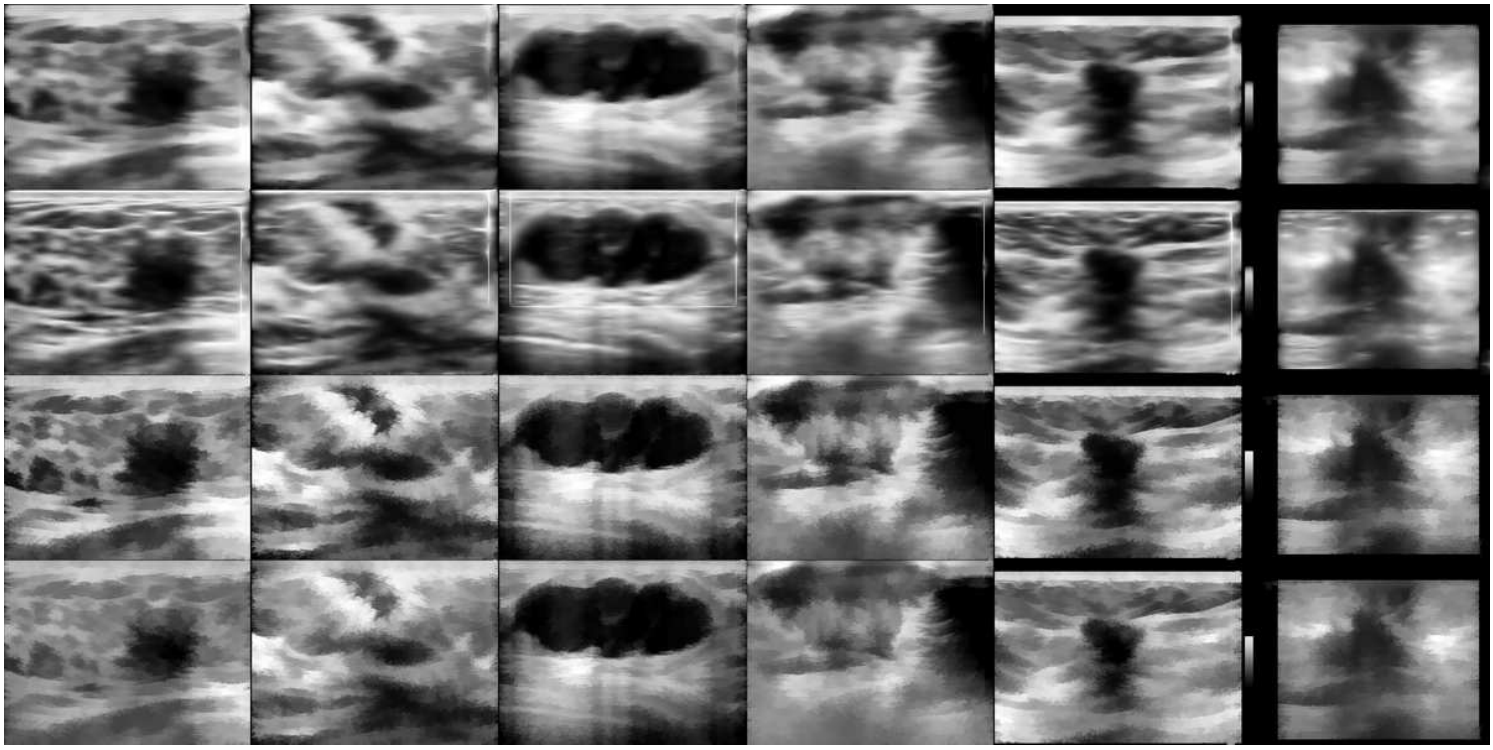

Figure 1

Some examples of the effect of different preprocess methods. From the first row to the last row are the result of CCS(contrast limited adaptive histogram equalization+curvature filter+side window filter), CC(contrast limited adaptive histogram equalization+curvature filte), CS(contrast limited adaptive histogram equalization+side window filter) and SWF(side window filter) respectively.

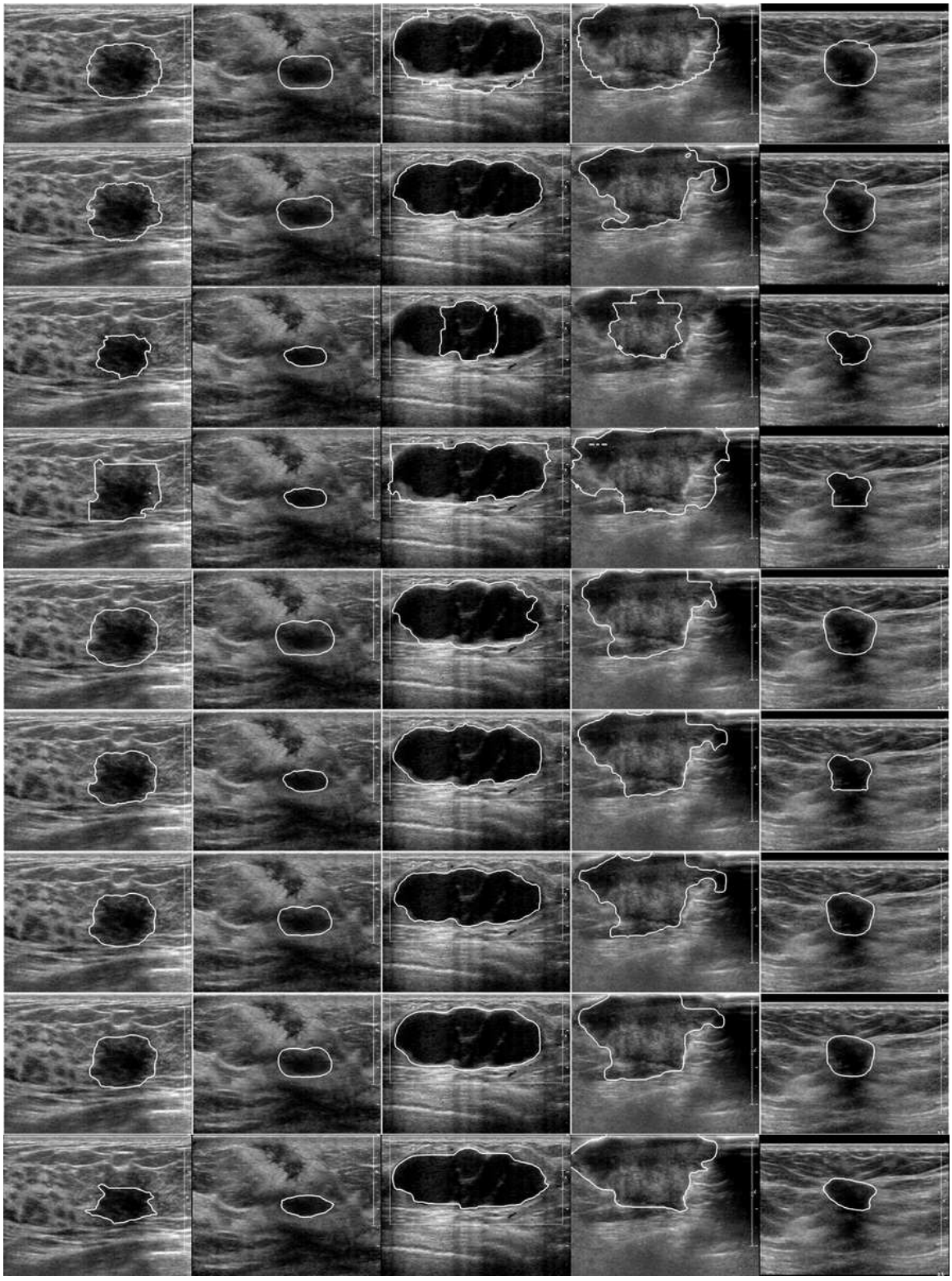

Figure 2

From up to down are the qualitative result of MW(markerd watershed), LST(level set), MS(morphological snake), AMS(adaptive morphological snake), MS+MW(morphological snake and marked watershed), AMSMW(Adaptive morphological snake and marked watershed), LST+MW(level set and marked watershed), FSMW and GT(ground truth)

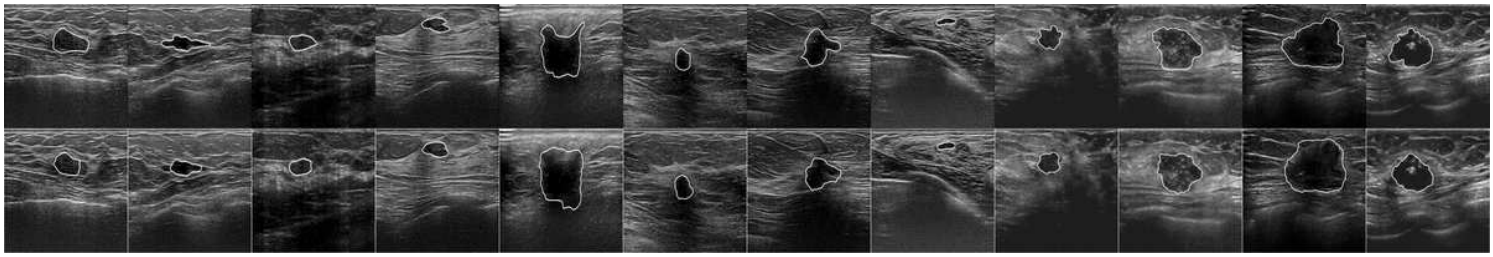

Figure 3

The qualitative segmentation result. The first row is GT and the second row is the qualitative result of AMSMW on the shared database. And from left to the right are image(a), image(b), image(c), image(d), image(e), image(f), image(g), image(h), image(i), image(j), image(k) and image(l). All of them can be found in the figure11,figure12 and figure 13 of Zhuang's paper ([22]) accordingly.

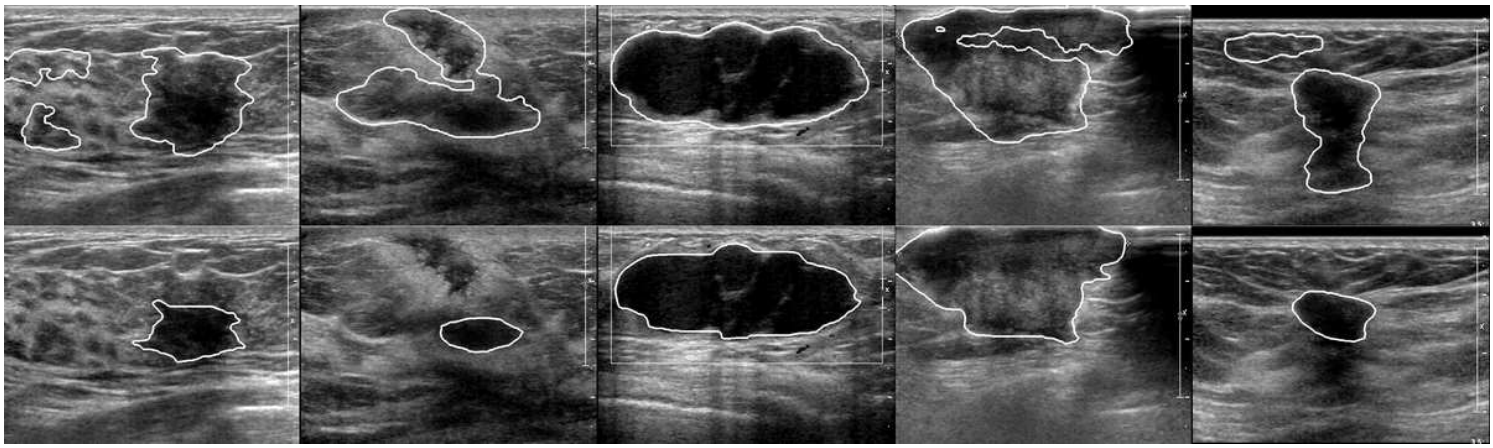

Figure 4

From up to down are the qualitative result of RADU-NET and GT, respectively.

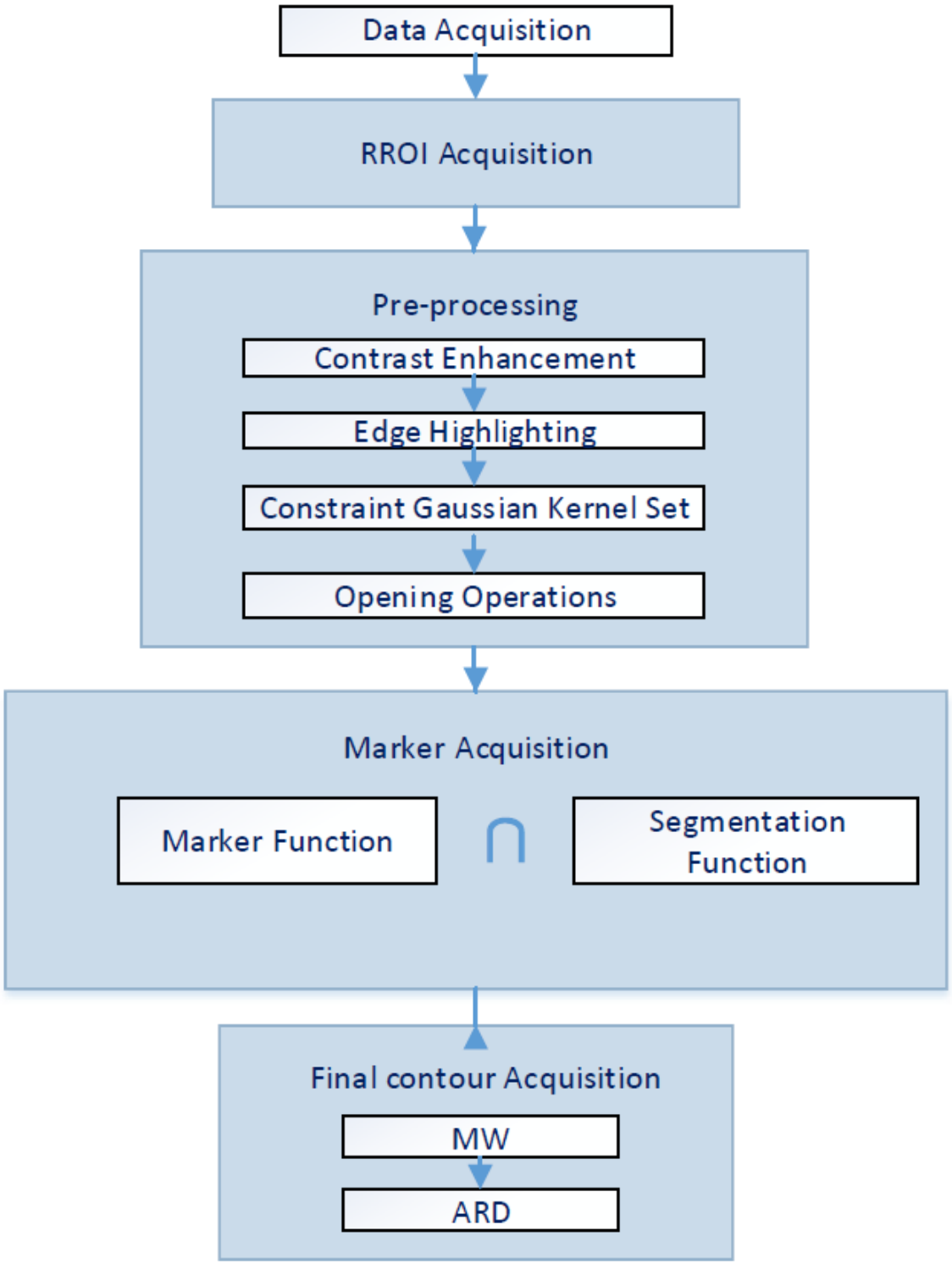

Figure 5

Flowchart of the proposed method

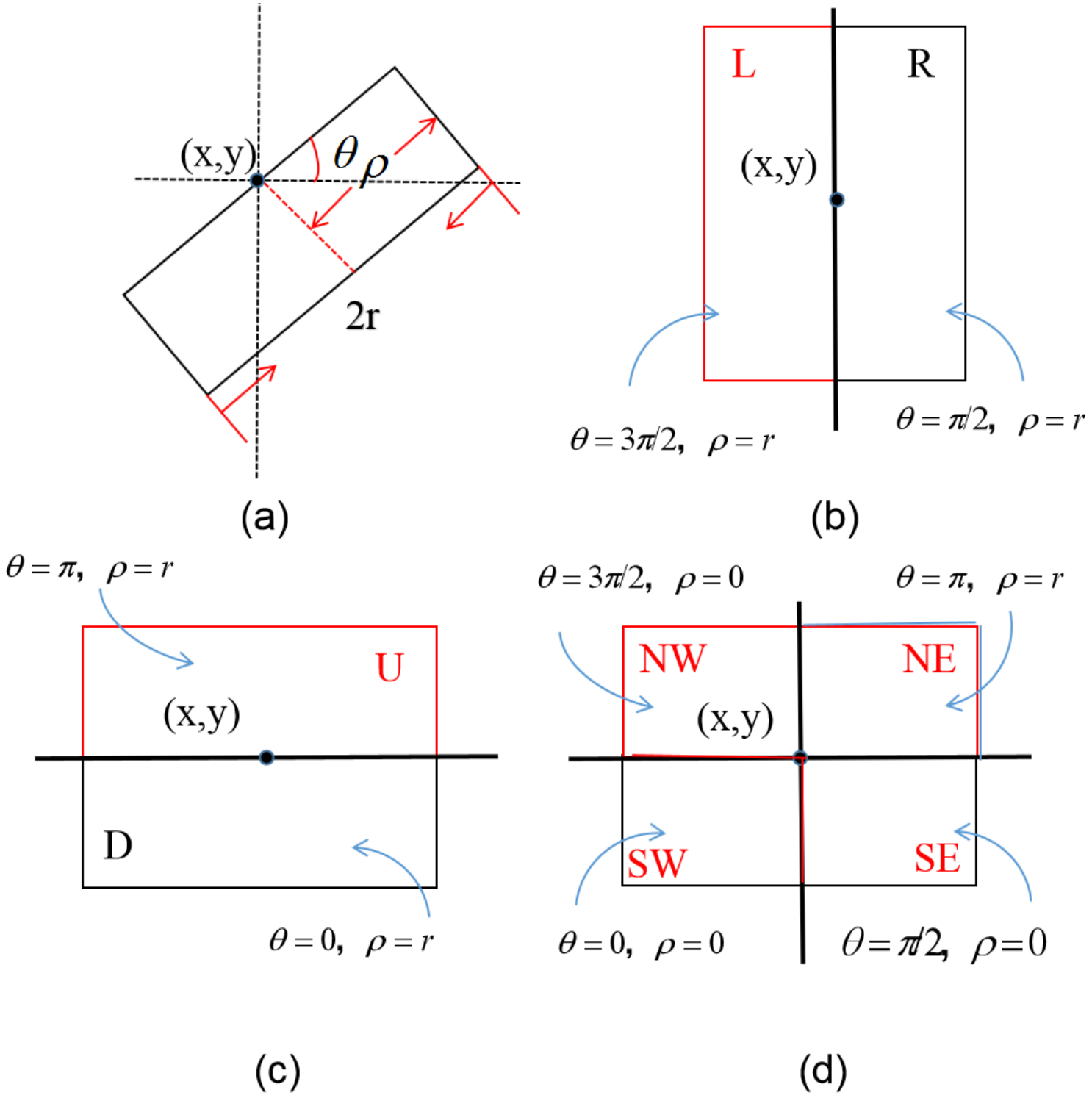

Figure 6

Definition of side window. r is the radius of the window. (a) side window in continuous case. (b) The left (L) and right (R) side window. (c) The up (U) and down (D) side window. (d) The northeast (NE), northwest (NW), southeast (SE) and southwest (SW) side window.

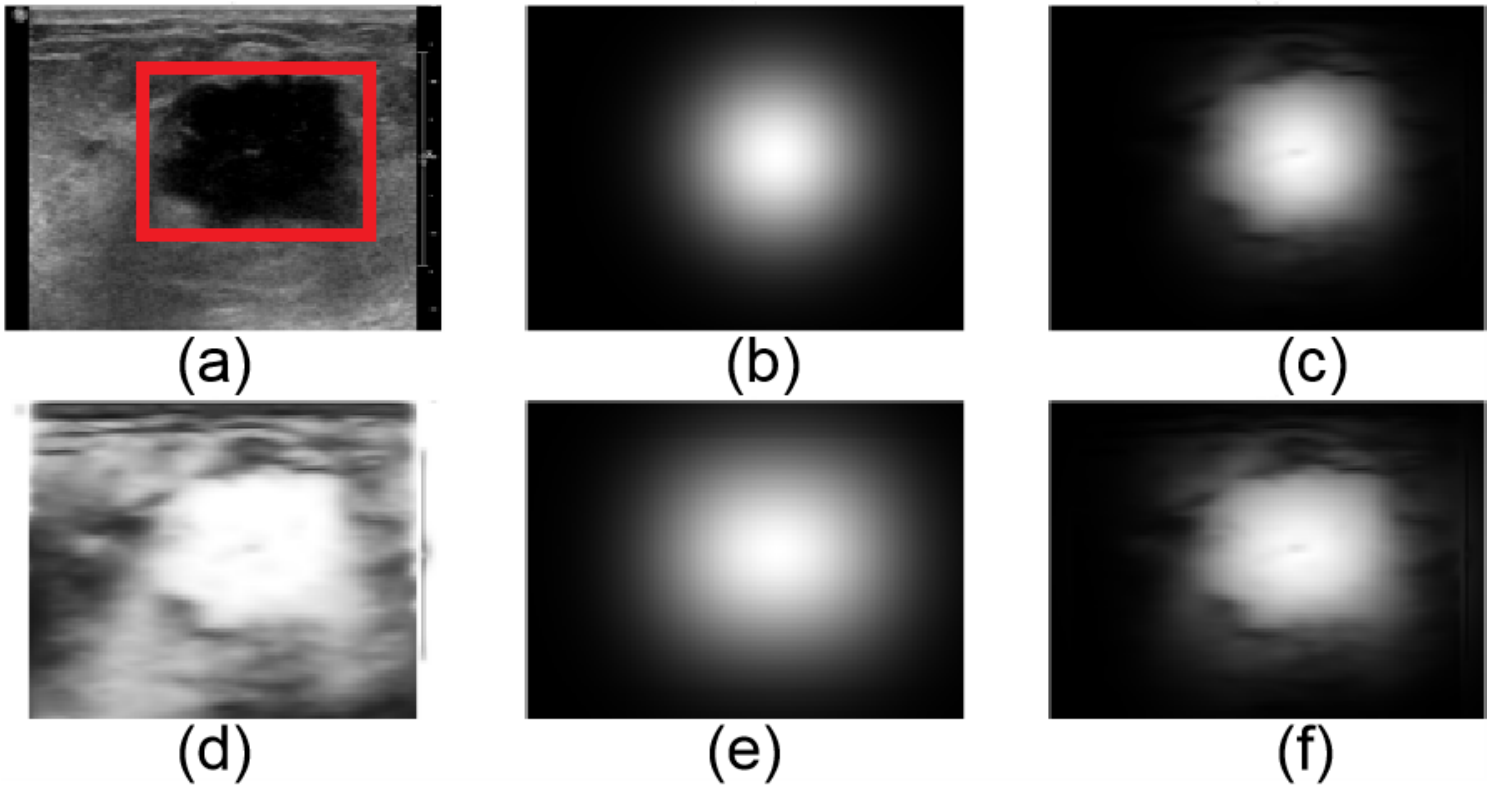

Figure 7

The process of obtaining ROI(region of interest). (a) original image with RROI(rectangle region of interest) draw by hands; (b) a constrained Gaussian function centered at the geometric center of RROI; (c) resultant image after multiplying (b) and (d); (d) negative of ICF ; (e) the union of five constrained Gaussian functions; (f)resultant image, which is denoted as J, after multiplying (e) and (d).

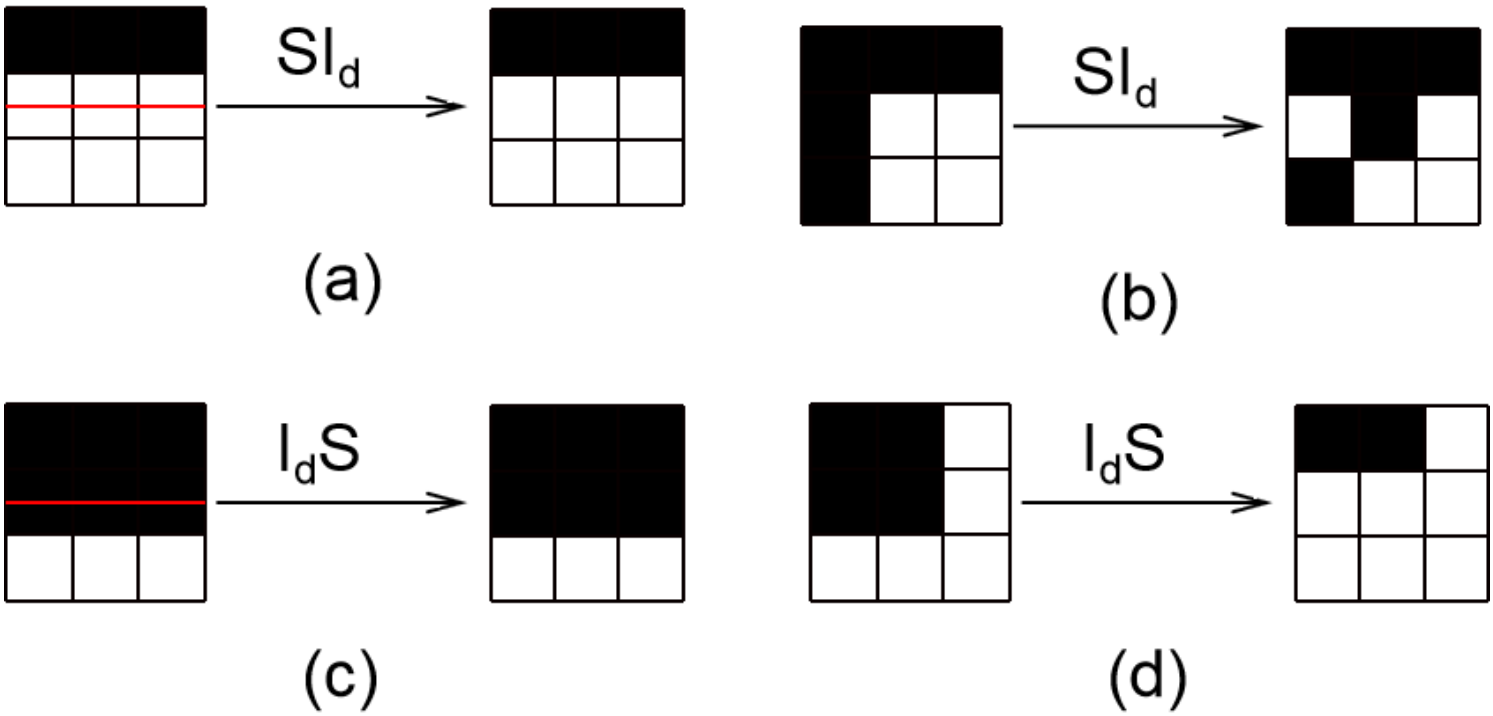

Figure 8

Some example of the effect of the SId and IdS operator. It keeps unchanged where a straight line(marked in red) is found, as shown in (a) and (c). However, when the center point isn't in any straight line, it will be changed as shown in (b) and (d)